01 May 2023

Machine Learning For A Vernier-effect-based Optical Fiber Sensor

Chen Zhu
Missouri University of Science and Technology, cznwq@mst.edu

Osamah Alsalman

Wassana Naku

Optics Letters

Machine learning for a Vernier-effect-based optical fiber sensor

Chen Zhu,[1,*] [ORCID] **Osamah Alsalman,**[2] **and Wassana Naku**[3]

[1] *Research Center for Optical Fiber Sensing, Zhejiang Laboratory, Hangzhou 311100, China*
[2] *Department of Electrical Engineering, College of Engineering, King Saud University, P.O. Box 800, Riyadh 11421, Saudi Arabia*
[3] *Department of Electrical and Computer Engineering, Missouri University of Science and Technology, Rolla, MO 65409, USA*
*chenzhu@zhejianglab.com

In recent years, the optical Vernier effect has been demonstrated as an effective tool to improve the sensitivity of optical fiber interferometer-based sensors, potentially facilitating a new generation of highly sensitive fiber sensing systems. Previous work has mainly focused on the physical implementation of Vernier-effect-based sensors using different combinations of interferometers, while the signal demodulation aspect has been neglected. However, accurate and reliable extraction of useful information from the sensing signal is critically important and determines the overall performance of the sensing system. In this Letter, we, for the first time, propose and demonstrate that machine learning (ML) can be employed for the demodulation of optical Vernier-effect-based fiber sensors. ML analysis enables direct, fast, and reliable readout of the measurand from the optical spectrum, avoiding the complicated and cumbersome data processing required in the conventional demodulation approach. This work opens new avenues for the development of Vernier-effect-based high-sensitivity optical fiber sensing systems. © 2023 Optica Publishing Group

Sensors with high sensitivity and resolution are always desired in scientific and engineering applications. In the field of optical fiber sensing, the Vernier effect has been demonstrated as an effective tool to improve the sensitivity of interferometric sensors in recent years [1–3]. Inspired by the Vernier caliper, the implementation of the optical Vernier effect requires the integration of two interferometers in a single system. The superposition of the signals of the two interferometers generates a Vernier envelope (typical amplitude modulation) at the output spectrum of the system. Instead of tracking the spectral fringe shifts of the individual interferometers, the Vernier envelope—whose shift is significantly magnified in response to external perturbations—is employed as the reference.

Recent efforts have mostly focused on the development of Vernier-effect-based optical fiber sensors based on different combinations of interferometers in parallel or in line. Examples include two Fabry–Perot interferometers (FPIs) [4–8], two Mach–Zehnder interferometers [9–11], and two Sagnac interferometers [12,13]. Hybrid systems with two different interferometers have also been reported [14,15]. Sensitivity-enhanced

sensing of a variety of physical and chemical parameters, such as temperature [16,17], strain [18,19], refractive index [20,21], biomarkers [22,23], etc., has been successfully realized based on the Vernier effect. The interrogation of a Vernier-effect sensor requires a broadband light source (e.g., a superluminescent diode, SLD) and an optical spectrum analyzer (OSA) to measure the spectral response over a broad range of wavelengths. Cumbersome and additional signal processing is required to extract the Vernier envelope, which is then correlated to the parameter of interest. The signal processing typically involves locating the fringe dips in the superimposed spectrum and applying a nonlinear curve fit to the discrete dip points to obtain the Vernier envelope, as detailed in Ref. [24]. This multi-step processes could introduce additional errors and thus ultimately deteriorate the performance of the sensor system. Indeed, rich information is contained in the superimposed spectrum, but the conventional analysis method only takes advantage of a few data points, thus compromising the capability of the sensor. On the other hand, machine learning has been employed in the field of optical sensing very recently [25–27]. By using the global features (i.e., the full spectrum) in combination with ML analysis, a higher measurement accuracy and expanded functionality were demonstrated for simple optical fiber sensors, which would have been challenging to achieve based on the conventional single fringe-dip tracking approach.

In this Letter, we propose and demonstrate an ML-based demodulation method for optical-Vernier-effect-based optical fiber sensors. The ML-based analysis directly uses the full information contained in the measured raw spectra and achieves one-to-one mapping between the measurand and the spectrum. A side-by-side comparison between the conventional approach and the ML-based method is given in Fig. 1. As a proof of concept, a Vernier-effect system based on two FPIs is employed and strain measurements are performed. Figure 2(a) gives the schematic of the experimental setup.

The FPI device is fabricated by a three-step process. A section of a capillary is first fusion spliced to a lead-in fiber, followed by high-precision cleaving under a microscope. Finally, the free end of the capillary with the lead-in fiber is spliced with a lead-out fiber. Figure 2(b) shows the measured interference signals of the individual FPIs. Modulation envelopes are observed in the measured raw spectra of the two FPIs, due to the co-existence of the antiresonance (AR) guidance that occurred in the capillary
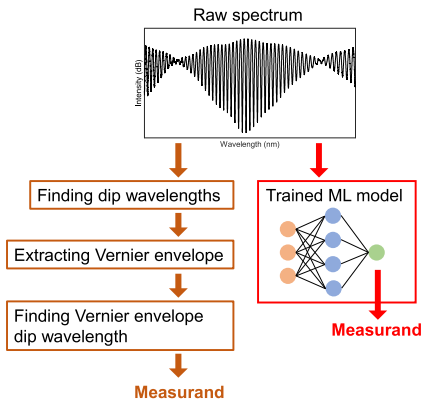
Fig. 1. Side-by-side comparison between the conventional method and the proposed ML method for the demodulation of a Vernier-effect sensor.
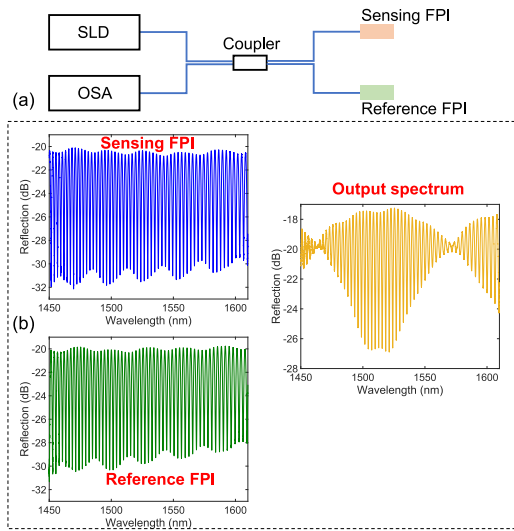

Fig. 2. System characterization. (a) Schematic of system implementation. (b) Measured spectra of the individual interferometers and the system output.

[28]. The cavity lengths of the sensing FPI and reference FPI are found to be 414.70 µm and 404.08 µm, respectively. The sensitivity magnification factor can be calculated based on [1]

$$M = \frac{OPD_{sen}}{OPD_{sen} - OPD_{ref}}, \tag{1}$$

where OPD_{sen} and OPD_{ref} denote the optical path differences of the sensing FPI and the reference FPI, respectively. Based on Eq. (1), the expected sensitivity magnification is 39.

The output spectrum of the system is included in Fig. 2(b). A Vernier envelope modulation signal is obtained, as expected. Slight distortions are observed due to the AR-induced irregular envelopes in the individual spectra from the two FPIs. In particular, the envelope dip at ~1510 nm exhibits irregular shapes, which could introduce additional errors into the process of locating the envelope dip wavelength. The free spectral range (FSR) is found to be approximately 110 nm, ~39 times larger than the FSR of the sensing FPI. By tracking the spectral shift of the Vernier envelope, sensitivity-enhanced strain sensing can be realized.
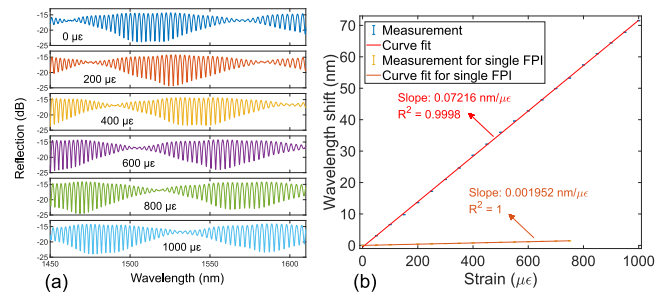

Fig. 3. Strain responses of the sensor based on the conventional demodulation method. (a) Exemplary spectral responses for different settings of the strain. (b) Vernier envelope dip wavelength as a function of strain, demonstrating sensitivity-enhanced sensing with a magnification factor of ~37.
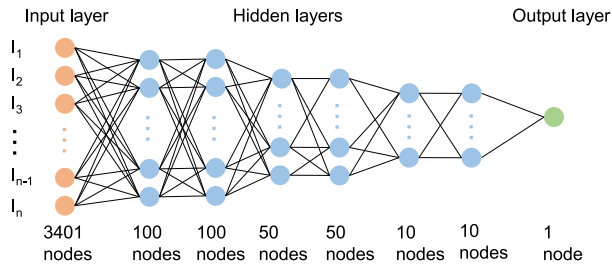
Tensile strains were applied to the sensing FPI by elongating the FPI fiber section using a motorized translation stage with a step resolution of 1 µm, corresponding to an applied strain accuracy of 5 µε considering that the two fixed points are 20 cm away during the strain experiment. Strains were incrementally applied in steps of 50 µε to a maximum of 1000 µε. The reference FPI was secured in a box to avoid external perturbations. Fifty measurements were performed at each setting of strain, i.e., 50 spectra were recorded. A total of 1050 spectra were obtained, with each spectrum including 4001 points that linearly span the range of 1450–1610 nm.

The strain responses of the system were first characterized using the conventional method to verify the sensitivity-enhanced sensing performance. A few exemplary output spectra are shown in Fig. 3(a). The Vernier envelope shifted to the long-wavelength regime with increasing strain. The determined Vernier envelope dip wavelength as a function of the tensile strain is plotted in Fig. 3(b). The measured responses of the sensing FPI without the Vernier effect are also included. The measurement sensitivities with and without the Vernier effect are determined to be 0.07216 nm/µε and 0.001952nm/µε, respectively, by means of linear curve fits, revealing a magnification factor of ~37. Thus, the functionality of the Vernier effect is demonstrated.

To further evaluate the performance of the conventional-method-based signal analysis, the strains are inversely derived from the determined Vernier envelope dip wavelengths based on the curve-fitting result shown in Fig. 3(b). Figure 4(a) shows the differences between the calculated strains and the applied strains. Relatively large deviations of up to 10 µε from the ground truth
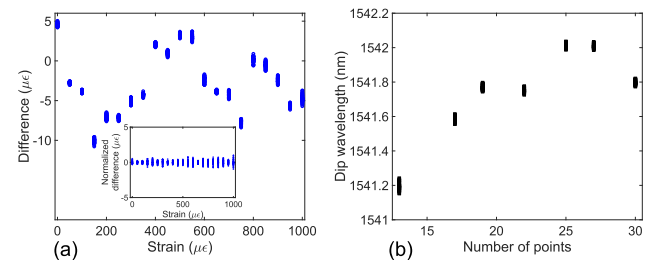
Fig. 4. Performance evaluation of the conventional curve-fitting method. (a) The difference between the derived strain and ground truth. The inset shows the normalized difference (normalized to the average value of 50 measurements for each strain setting). (b) The determined Vernier envelope dip wavelength with respect to the number of points used in the nonlinear curve fit.
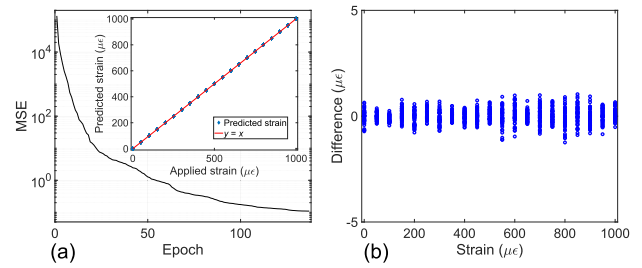
Fig. 5. Topological structure of the NN model for the Vernier sensor.

Fig. 6. Results from NN-based analysis. (a) MSE as a function of the epoch during the training process of the NN model. The inset shows the predicted strains with respect to the ground truth. The line $y = x$ is employed as the reference. (b) The differences between the predicted strains and the ground truth.

are observed. The inset shows the normalized difference. Meanwhile, while extracting the Vernier envelopes, we found that the number of points (discrete fringe dips in the output spectrum) that are used to fit the envelope signal is critically important and could cause ambiguity. Let's take the measured 50 spectra at a strain setting of 400 µε as an example. A Gaussian curve fit was applied to find the Vernier envelope. The determined dip wavelengths are plotted against the number of points used in the curve fit in Fig. 4(b). The dip wavelength varied by up to 0.8 nm when different numbers of points were used, corresponding to a strain variation of 11 µε. Thus, more reliable and consistent signal analysis approaches need to be explored to improve the performance of the Vernier sensor. Here, ML is applied.

The feedforward neural network (NN) is employed in this work as it has been demonstrated to be effective for processing signals from optical fiber sensors [25,29–31]. The NN model used in this work was configured with six hidden layers, and hidden layers 1 to 6 were included with 100, 100, 50, 50, 10, and 10 nodes after empirical validation. The output layer included one node, corresponding to the tensile strain. The activation functions used for the hidden layers and the output layer were sigmoid and linear, respectively. The aforementioned 1050 spectra were randomly split into training, validation, and test datasets with splitting ratios of 75%, 15%, and 15%. We noticed that a few data points in the starting wavelength and the end wavelength were quite noisy due to the low power from the SLD source used in the experiment. Thus, these data points were removed from the datasets used for training the NN. The input layer included 3401 nodes, corresponding to the 3401 sampling points in each of the optical spectra ranging from 1461.96 nm to 1597.96 nm. A schematic of the topological structure of the constructed NN is given in Fig. 5.

The mean squared error (MSE) as a function of the training epoch during the training process is plotted in Fig. 6(a). The MSE decreased rapidly initially and gradually stabilized after epoch 130. The predicted strains from the trained model with respect to the applied strains are shown in the inset of Fig. 6(a). As can be seen, the data points of the predicted strains are aligned close to the reference line $y = x$, indicating that the predicted values match well with the ground truth. The differences between the predicted strains and the applied strains are shown in detail in Fig. 6(b). Compared with the results obtained from the conventional method shown in Fig. 4(a), the NN-based analysis realized higher accuracy and more reliable prediction, with errors smaller than 1.1 µε. Meanwhile, since the raw spectra are used for input, the cumbersome pre-processing that could introduce ambiguity is avoided. Thus, the NN-based analysis is effective and efficient; the well-trained NN can extract the useful information contained in the raw spectra, and it consequently

achieves one-to-one mapping directly between a raw spectrum and the applied strain for the Vernier sensor.

Considering that the NN-based analysis uses the global features included in the raw spectrum instead of a single feature (e.g., the Vernier envelope dip wavelength), we expect that with the NN as the tool, the spectral interrogation bandwidth of the Vernier sensor could be further reduced even without covering the dip wavelength. This is important for developing new generations of Vernier-effect-based sensor systems, as a smaller-bandwidth source is lower in cost, and the spectrum sampling points could be reduced due to the reduced wavelength range, which could lead to the development of dynamic Vernier sensors. To this end, we extract the data points in the 1050 collected spectra within the wavelength range of 1528–1563 nm, corresponding to the wavelength bandwidth of a C-band light source. The number of sampling points for each revised spectrum is 876. A few revised spectra are shown in Fig. 7(a), which show that the Vernier envelope dips are not covered due to the limited wavelength range. A new NN model was constructed, similar to the one shown in Fig. 5. The only difference was that the input layer for the new model included
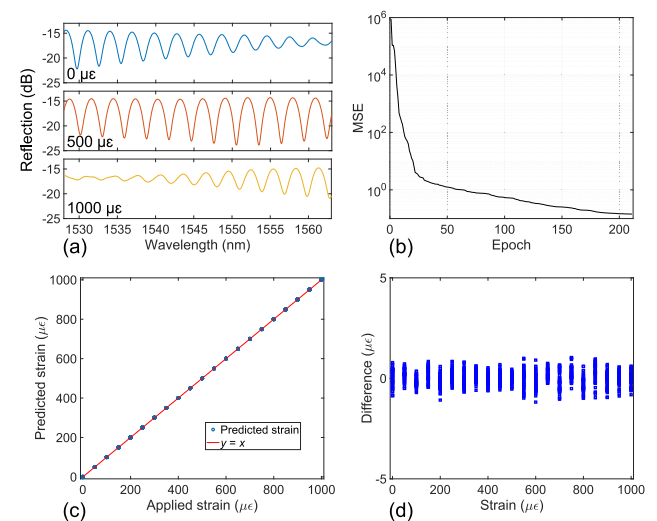
Fig. 7. Results from NN-based analysis when the wavelength range of the spectra is reduced to 1528 nm to 1563 nm. (a) Exemplary spectra for different settings of the strain. (b) MSE during the training process. (c) Comparison between the predicted strains and the applied strains. (d) Difference between the predicted strains and the applied strains.

876 nodes, corresponding to the 876 sampling points for each revised spectrum. Figure 7(b) gives the obtained MSE as a function of the epoch during the training process of the new NN model, showing that the model converged rapidly. A comparison between the predicted strains and the applied strains is shown in Fig. 7(c). A detailed view of the differences between the predicted and applied strains is given in Fig. 7(d). Compared with the results shown in Fig. 6, we can conclude that the performance of the NN analysis does not deteriorate when the sampling points for each spectrum are significantly decreased. Note that for the case where the dip for the Vernier modulation envelope is not included in the measured spectrum, it would have been challenging, if not impossible, to extract useful information if the conventional method were employed. Thus, it is possible to employ a coarsely resolved highspeed spectrometer and a light source with limited wavelength bandwidth to develop a faster, cheaper, and simpler interrogator for Vernier sensors. A performance comparison between the conventional dip tracking method and the ML approach can be found in Table 1 in Supplement 1.

To conclude, we have proposed and demonstrated a new method for demodulating signals of Vernier-effect-based optical fiber sensors based on ML. As a proof of concept, a Vernier sensor system based on two FPIs was employed in the experiment. It was shown that the NN model can be trained to predict the strains applied on the sensing FPI directly based on the measured raw spectrum with high consistency and reliability, remarkably outperforming the conventional dip tracking method. More importantly, the prediction accuracy does not degrade when the wavelength range of the measured raw spectrum is decreased significantly; even when it does not cover the dominant feature, i.e., the envelope dip. This work represents a novel attempt to advance Vernier sensors and opens up a new direction in the development of high-sensitivity Vernier sensor systems.

Disclosures. The authors declare no conflicts of interest.

Data availability. Data underlying the results presented in this paper are not publicly available at this time but may be obtained from the authors upon reasonable request.

Supplemental document. See Supplement 1 for supporting content.

REFERENCES

1. A. D. Gomes, H. Bartelt, and O. Frazão, Laser Photonics Rev. **15**, 2000588 (2021).
2. Y. Liu, X. Li, Y.-n. Zhang, and Y. Zhao, Measurement **167**, 108451 (2021).
3. Y. Chen, L. Zhao, S. Hao, and J. Tang, Sensors **22**, 2694 (2022).
4. Y. Zhao, P. Wang, R. Lv, and X. Liu, J. Lightwave Technol. **34**, 5351 (2016).
5. L. G. Abbas, IEEE Sens. J. **20**, 12384 (2020).
6. J. Tian, Z. Li, Y. Sun, and Y. Yao, J. Lightwave Technol. **37**, 5609 (2019).
7. T. Paixão, F. Araújo, and P. Antunes, Opt. Lett. **44**, 4833 (2019).
8. C. Zhu and J. Huang, Opt. Express **29**, 16820 (2021).
9. M. Xie, H. Gong, J. Zhang, C.-L. Zhao, and X. Dong, Appl. Opt. **58**, 6204 (2019).
10. Y. Zhao, H. Lin, C. Zhou, H. Deng, A. Zhou, and L. Yuan, IEEE Photonics Technol. Lett. **31**, 591 (2019).
11. H. Lin, F. Liu, Y. Dai, and A. Zhou, IEEE Sens. J. **19**, 2581 (2019).
12. L.-Y. Shao, Y. Luo, Z. Zhang, X. Zou, B. Luo, W. Pan, and L. Yan, Opt. Commun. **336**, 73 (2015).
13. S. Liu, G. Lu, D. Lv, M. Chen, and Z. Zhang, Opt. Fiber Technol. **66**, 102654 (2021).
14. L. Liu, T. Ning, J. Zheng, L. Pei, J. Li, J. Cao, X. Gao, and C. Zhang, Opt. Laser Technol. **119**, 105591 (2019).
15. X. Jia, X. Zhou, M. Bi, G. Yang, M. Hu, and T. Wang, Opt. Fiber Technol. **65**, 102625 (2021).
16. F. Wang, Y. Liu, Y. Lu, L. Zhang, J. Ma, L. Wang, and W. Sun, Opt. Lett. **43**, 5355 (2018).
17. A. D. Gomes, M. Becker, J. Dellith, M. I. Zibaii, H. Latifi, M. Rothhardt, H. Bartelt, and O. Frazão, Sensors **19**, 453 (2019).
18. J. Deng and D. Wang, J. Lightwave Technol. **37**, 4935 (2019).
19. P. M. R. Robalinho, A. D. Gomes, and O. Frazao, IEEE Photonics Technol. Lett. **32**, 1139 (2020).
20. Z. Xu, Q. Sun, B. Li, Y. Luo, W. Lu, D. Liu, P. P. Shum, and L. Zhang, Opt. Express **23**, 6662 (2015).
21. Z. Xu, Y. Luo, D. Liu, P. P. Shum, and Q. Sun, Sci. Rep. **7**, 1 (2017).
22. L. Chen, J. Li, F. Xie, J. Tian, and Y. Yao, J. Lightwave Technol. (2023).
23. K. Li, N. Zhang, N. M. Y. Zhang, W. Zhou, T. Zhang, M. Chen, and L. Wei, Sens. Actuators, B **275**, 16 (2018).
24. Y. Li, Y. Li, Y. Liu, Y. Li, and S. Qu, Opt. Express **30**, 35734 (2022).
25. L. V. Nguyen, C. C. Nguyen, G. Carneiro, H. Ebendorff-Heidepriem, and S. C. Warren-Smith, Photonics Res. **9**, B109 (2021).
26. B. Duan, H. Zou, J.-H. Chen, C. H. Ma, X. Zhao, X. Zheng, C. Wang, L. Liu, and D. Yang, Photonics Res. **10**, 2343 (2022).
27. C. Zhu and J. Huang, Opt. Express **30**, 24553 (2022).
28. X. Zhang, H. Pan, H. Bai, M. Yan, J. Wang, C. Deng, and T. Wang, Opt. Lett. **43**, 2268 (2018).
29. L. Avellar, A. Frizera, H. Rocha, M. Silveira, C. Díaz, W. Blanc, C. Marques, and A. Leal-Junior, Photonics Res. **11**, 364 (2023).
30. C. Zhu, Y. Zhuang, and J. Huang, J. Lightwave Technol. **40**, 5762 (2022).
31. C. Zhu, H. Deng, Z. Ding, J. Huang, and Z. Zhang, Opt. Lett. **46**, 5838 (2021).